Ultraviolet-wavelength driven solar spectral converter for photovoltaic cell application

Pei Song, * **Chaomin Zhang, and Pengfei Zhu**

Shanghai University of Engineering Science, School of Mathematics, Physics and Statistics, Shanghai, China

ABSTRACT. Realizing an excellent spectral response by utilizing the ultraviolet parts of solar radiation is an important focus for enhancing the performance of photovoltaic cells (PCs). Pr^{3+} and Eu^{3+} ions co-doped multifunctional transparent $GdPO_4$ glass-ceramic is successfully prepared using a conventional melting quenching technique. In $GdPO_4$: Pr^{3+}-Eu^{3+}, ultraviolet to visible downshifting is realized via the remarkable energy transfer from Pr^{3+} to Eu^{3+} ions by bridge Gd^{3+} ions. Introducing the spectral conversion material by converting ultra-violet photons into visible photons is considered a very promising route; it can be applied to perovskite PCs by reducing the photo-degradation and enhancing the light harvesting, and it can be applied to hydrogenated amorphous-silicon carbide PCs by reducing the solar energy losses associated with spectral mismatch of the spectral response and energy. The development of downshifting Pr^{3+}-Eu^{3+} co-doped glass-ceramics might open up a new approach to achieving a better performance of photovoltaic devices.

© 2023 Society of Photo-Optical Instrumentation Engineers (SPIE) [DOI: 10.1117/1.JPE.14.015501]

Keywords: down-shift; stability enhancement; glass-ceramic; a-SiC: H; perovskite; photovoltaic cell

1 Introduction

Global energy demands have created increasing attention to solar energy sources. Unfortunately, at present, the low efficiency of "light-to-electricity" transformation leads to the high cost of generated energy.[1,2] Perovskite photovoltaic cells (PPCs) have recently been considered to be promising novel photovoltaic cells (PCs) for solar energy because of their broader light-absorption and higher efficiencies.[3–11] Solar radiation contains wide wavelengths ranging from ultraviolet (UV) to near-infrared (NIR), but current PPCs only utilize a relatively small part of this spectrum, as shown in Fig. 8(a). A major problem limiting the power conversion efficiency (PCE) of PPCs is their insensitivity to the whole solar spectrum. PPCs have a degradation problem due to various environmental factors including moisture, temperature, and oxygen. But the major problem of degradation of PPCs is due to UV light exposure, which causes PPCs to suffer from a deep trapping of injected electrons within newly available sites in the PPCs and a loss of charge in PPCs.[6,7,12] Because the degradation of the PPCs is mainly caused by the intensity of UV, it may be mitigated by some preparation techniques, such as UV filters. Hydrogenated amorphous-silicon carbide PCs (a-SiC: H PC) are also widely used, but they cannot effectively harvest UV photons because of the mismatch between the sunlight radiation and the spectral response (SR) of a-SiC:H materials.[13,14] Decreasing the UV light in solar radiation can enhance the light stability of PPCs. Applying downshifting (DS) effects to PPCs can prevent UV photons of solar radiation to interact with the perovskite photo-active layer by converting them into

---

*Address all correspondence to P. Song, psong@sues.edu.cn

visible (VIS) photons and enhance the photo-current with improved light stability for high energy UV photons. To reduce the solar energy losses associated with the spectral mismatch of SR and energy distribution in the solar spectrum, applying DS effects can convert UV light to VIS light and help to enhance the absorption of a-SiC:H PCs.[15–24] The rare earth (RE) doped transparent hosts are promising spectral conversion materials (SCMs) for this role due to their excellent thermal, mechanical, and optical properties.[1,25–28] In particular, the RE multi-doped glass-ceramic (GC) is a perspective candidate for this purpose. As a kind of RE doped organophosphate material, $GdPO_4$ has unique properties and has been widely investigated in recent years. With seven unpaired electrons, Gd^{3+} ion is a suitable substitution site for doping RE ions that could be exploited in designing new functional luminescence materials. Moreover, $GdPO_4$ exhibits high thermal and chemical stabilities, which are required for luminescence materials. In this paper, we investigate the potential use of $GdPO_4$-GC: Eu^{3+}/Pr^{3+} synthesized by the melting quenching (MQ) process. This novel, efficient, and stable SCM was selected to extend the SR range of PCs to the UV region with the goal of enhancing the performance of PCs. It possesses a broad band absorption in the UV range and re-emits VIS photons, which could improve the photo-current and PCE, accompanied by greatly enhanced light and UV stability of PCs. PCs are necessary in space stations and artificial satellites. The solar spectrum in space shows strong UV absorption ranging from 200 to 300 nm.[29] For space PCs, our SCMs can be used as a promising protective layer for simultaneously preventing thermalization and enhancing the PCE.[30–32]

2 Experimentation

The SCM selected for this work has relative high emission efficiencies and absorbs UV radiation and converts the wavelength to one that is closer to the SR of the PC. The SCM was selected to ensure that optical absorption is in the UV region of solar radiation and its luminescent emission occurs at wavelengths for which the PC has a high SR. The relevant aspects to selecting the SCM were its optical property, processability, and inexpensiveness. The glass samples with mol. % compositions $40SiO_2 + 22Al_2O_3 + 20Na_2CO_3 + 4NaF + 6P_2O_5 + 8GdF_3$ were prepared by the MQ method with the high purity reagent grade SiO_2, Al_2O_3, Na_2CO_3, NaF, P_2O_5, and GdF_3 as raw materials. Pr_4O_7 and Eu_2O_3 were used as RE dopants with doping levels of $xPr^{3+} - yEu^{3+}$ mol. %, where $x = 2$ and $y = 1$. The batches weighing about 0.015 kg were melted at 1500°C in air for 1 h in a corundum crucible, poured onto a pre-heated brass plate, and then pressed by another plate. Then, the molten glasses were annealed at 460°C for 7 h. Finally, the glasses were heat-treated at 670°C for 1.5 h to form the GC samples. The obtained GC samples were cut, polished to 350 mm × 350 mm × 2 mm (~5 mm), and subjected to optical measurements. Absorption spectra ranging from 200 to 800 nm were collected by a UV/VIS/NIR spectrophotometer (UV-3600, Shimadzu, Japan). The photoluminescence (PL), photoluminescence excitation, and DS emission spectra of the GC samples were performed on an Omni-SBP-λ300 fluorescence spectrophotometer (Zolix Corp., China) under the excitation of an LHX500 xenon arc lamp (Zolix Corp., China) and 486 nm laser diode (Zolix Corp., China). The VIS emission was detected using a photomultiplier tube detector. To eliminate the noise from the excitation lamp, different filters were put before the detector. The whole experiments were carried out at 25°C.

For this work, the configuration consisted of the incident light facing the side of the PC being covered with a prepared GC sample, which allowed the DS photons to be harvested without interfering with the SCM, as shown in Fig. 1. The advantage of using this structure is that the filter and the PC can be designed independently, the covered filter will not damage the structure of the PC itself, and the filter can be applied to other PCs, if applicable. The disadvantage is possibly low optical coupling between the filter and the PC at the interface due to the difference in the refractive index. The PPC module is the combination of the real cell and fluorine-doped tin oxide (FTO) as the top electric contact.[12] The structure of a-SiC: H-PC is a glass/SnO_2/p a-SiCH/i-n a-Si: H/Al substrate with heteroface type. These two kinds of PCs have the same side of 300×300 mm², which is slightly smaller than the GC sample to ensure that cells are completely covered. The GC was attached to the cell modules with index matching liquid immersion oil (IMLIO, Type 300, Nikon) to reduce the light loss. To value the effect of the cell
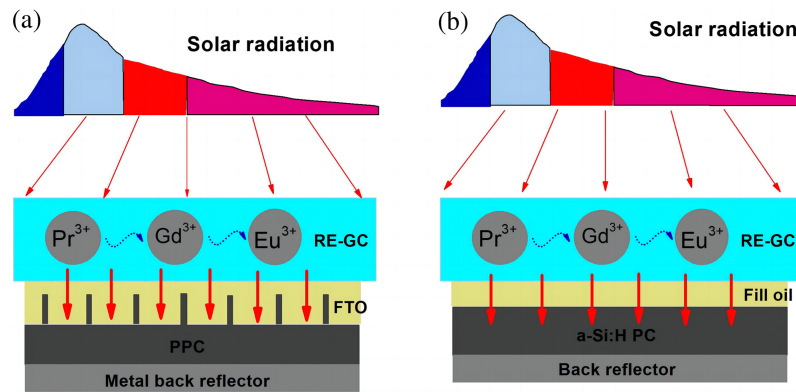
Fig. 1 Schematic diagram of $GdPO_4$ GC: Eu^{3+}/Pr^{3+} conversion layer for (a) PPC and (b) a-SiC: H PC.

modules' performances with GC samples, current–voltage (I-V) measurements were taken with an AM 1.5 Sunlight simulator (Keithley-2400).
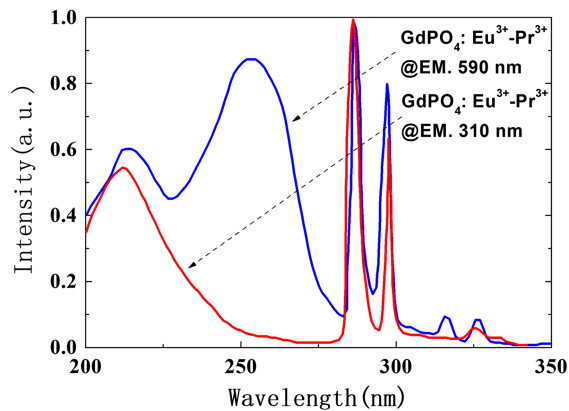
3 Results and Discussion

The GC sample that we used is 2 mm thick. The excitation spectrum of the GC sample by monitoring at the 590 nm emission of $GdPO_4$: Eu^{3+} and the excitation spectrum of the GC sample by monitoring at the 310 nm emission of host-$GdPO_4$ are shown in Fig. 2. In the excitation spectra of host-$GdPO_4$, the 310 nm emission is due to the transition of Gd^{3+}: $^6I_J \rightarrow {}^8S_{7/2}$, and the 250 and 275 nm narrow-bands are ascribed to the transitions of Gd^{3+}: $^8S_{7/2} \rightarrow {}^6D_J$ and Gd^{3+}: $^8S_{7/2} \rightarrow {}^6I_J$, respectively. In the excitation spectrum of $GdPO_4$: Eu^{3+}, the 590 nm emission is due to the transition of Eu^{3+}: $^5D_0 \rightarrow {}^7F_1$. Compared with the excitation spectrum of host-$GdPO_4$, in the excitation spectrum of $GdPO_4$: Eu^{3+}, the charge transfer band (CTB) of O^{2-} and Eu^{3+} from 200 to 270 nm covers the 250 nm narrow absorption peak of the Gd^{3+}: $^8S_{7/2} \rightarrow {}^6D_J$ transition.

The excitation spectra of GC samples by monitoring at the 590 and 310 nm emissions of $GdPO_4$: Eu^{3+}-Pr^{3+}, respectively, are exhibited in Fig. 3. In these two curves, we find that the 275 nm narrow-band and around 220 nm broad-bands are ascribed to the transitions of Gd^{3+}: $^8S_{7/2} \rightarrow {}^6I_J$ and excitation peak of Pr^{3+}: 4f5d. In the excitation curve monitoring at the 590 nm emission, the CTB of O^{2-} and Eu^{3+} and the excitation band of Pr^{3+}: 4f5d are overlapping in the region of 200 to 220 nm. Compared with the excitation curve monitoring at the 310 nm emission, we can identify that the CTB of O^{2-} and Eu^{3+} is located near the 200 to 280 nm region. Figure 3
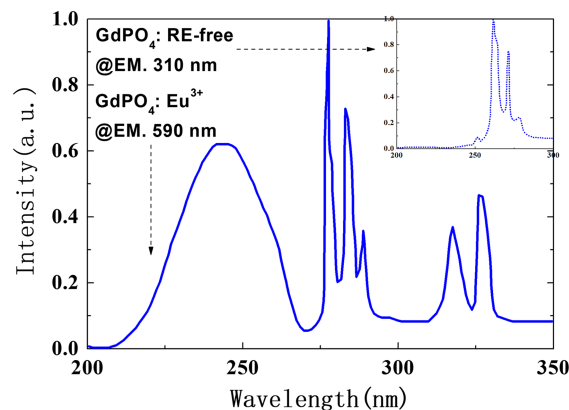
Fig. 2 Excitation spectrum (blue solid line) of the GC sample (2 mm thick) by monitoring at the 590 nm emission of $GdPO_4$: Eu^{3+}. Inset shows the excitation spectrum (blue dotted line) of the GC sample (2 mm thick) by monitoring at the 310 nm emission of host $GdPO_4$.
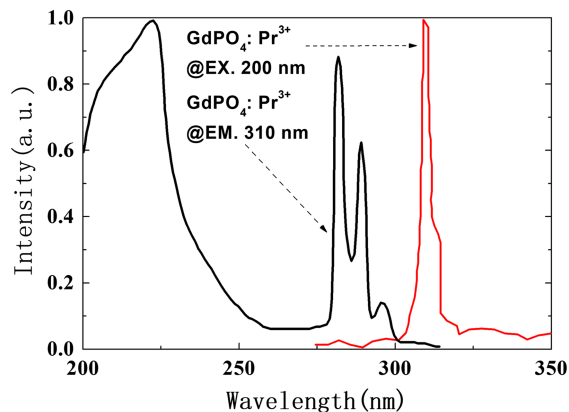
Fig. 3 Excitation spectra of GC samples (2 mm thick) by monitoring at the 590 nm (blue solid line) and 310 nm (red solid line) emission of $GdPO_4$: Eu^{3+}-Pr^{3+}, respectively.

clearly shows that the excitation band of Pr^{3+}: 4f5d contributes to the emission bands of both the Eu^{3+} and Gd^{3+} ions.
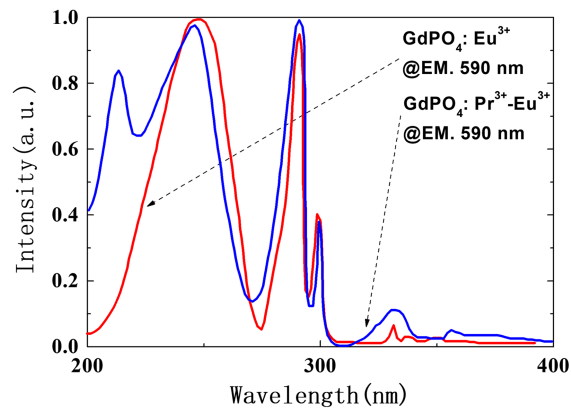
The excitation spectrum of the GC sample by monitoring at the 310 nm emission of $GdPO_4$: Pr^{3+} and the emission spectrum of the GC sample under the 200 nm excitation of $GdPO_4$: Pr^{3+} are shown in Fig. 4. In the excitation spectra of host-$GdPO_4$: Pr^{3+}, the 310 nm emission is due to the transition of Gd^{3+}: $^6I_J \rightarrow {}^8S_{7/2}$, and the 275 nm narrow-band is ascribed to the transition of Gd^{3+}: $^8S_{7/2} \rightarrow {}^6I_J$. The excitation band of Pr^{3+}: 4f5d contributes to the emission band of Gd^{3+} ions because the excitation curve of the GC sample by monitoring at the 310 nm emission of $GdPO_4$: Pr^{3+} and the excitation curve of GC samples by monitoring at the 310 nm emission of $GdPO_4$: Eu^{3+}-Pr^{3+} have the same shape. The PL curve of Pr^{3+}: 4f5d does not occur in the emission spectrum of the GC sample under the 200 nm excitation of $GdPO_4$: Pr^{3+} although 200 nm locates in the excitation band of Pr^{3+}: 4f5d, which reveals that the Pr^{3+} ion could sensitize the Gd^{3+} ion efficiently and puts almost all of its energy transfer (ET) into the Gd^{3+} ion.

Figure 5 shows the excitation spectra of GC samples by monitoring at the 590 nm emission of $GdPO_4$: Eu^{3+} and $GdPO_4$: Eu^{3+}-Pr^{3+}. The 220 nm region is ascribed to the excitation peak of Pr^{3+}: 4f5d, and the 200 to 220 nm region belongs to the CTB.

We used 220 nm as the pump wavelength to realize that the PL comes completely from the Pr^{3+} ion. The emission spectrum of the GC sample under the 220 nm excitation of $GdPO_4$: Pr^{3+}-Eu^{3+} is described in Fig. 6. The PL curve of Pr^{3+}: 4f5d is not observed in the emission spectrum of the GC sample under the 220 nm excitation of $GdPO_4$: Pr^{3+}, although 220 nm locates in the excitation band of Pr^{3+}: 4f5d. It can be observed that the transitions of Gd^{3+}:

Fig. 4 Excitation spectrum of the GC sample (2 mm thick) by monitoring at the 310 nm emission of $GdPO_4$: Pr^{3+} (black solid line) and the emission spectrum of the GC sample under 200 nm excitation of $GdPO_4$: Pr^{3+} (red solid line).

Fig. 5 Excitation spectra of GC samples (2 mm thick) by monitoring at the 590 nm emission of GdPO$_4$: Eu^{3+} (red solid line) and GdPO$_4$: Eu^{3+}-Pr^{3+} (blue solid line), respectively.
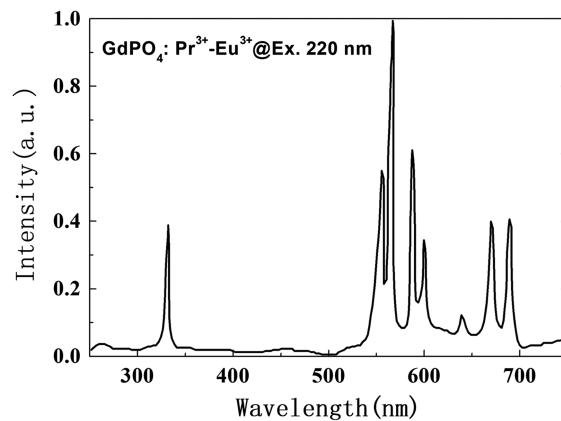

**Fig. 6** Emission spectrum of the GC sample (2 mm thick) under 220 nm excitation of GdPO$_4$: Pr^{3+}-Eu^{3+}.

$^6I_J \rightarrow {}^8S_{7/2}$ and Eu^{3+}: $^5D_0 \rightarrow {}^7F_J$ lead to the characteristic emission peaks centered at 310 and 590 nm, respectively. By looking at the emission spectrum of GdPO$_4$: Eu^{3+}, the Gd^{3+} ion puts most of its ET into the Eu^{3+} ion. In GdPO$_4$: Pr^{3+}-Eu^{3+}, by comparing the emission spectra of GdPO$_4$: Pr^{3+} and GdPO$_4$: Pr^{3+}-Eu^{3+}, we find that the ET from the Pr^{3+} ion to the Eu^{3+} ion by the bridge Gd^{3+} ion is more efficient than the direct ET between the Pr^{3+} ion and the Eu^{3+} ion. The Gd^{3+} ion could transfer most of its energy to the Eu^{3+} ion, and the Eu^{3+} ion emits the main peak of 590 nm by a downward transition from the $^5D_0$ state, as shown in Fig. 7.

We evaluated the benefits for cell devices equipped with the Pr^{3+}-Eu^{3+}-doped GC samples performance in an air-conditioned laboratory with a temperature of 20°C to 25°C and relative humidity level of 30% to 40%. The measured current density-voltage plots of cell devices at $t = 0$ h under AM1.5G simulated sunlight with 100 mW/cm^2 of irradiance for PCs with the RE-GC layer and with the RE-free GC layer is shown in Figs. 8(a) and 8(b). As the GC layer emits strongly in the VIS region (see Fig. 8, inset, red line), for PCs, this matching of the PL emission band of GdPO$_4$-GC: Eu^{3+}/Pr^{3+} with the absorbance bands of PCs in the VIS region establishes that the DS-GC is providing additional VIS photons, which is absorbed by PCs, giving rise to the photo-current increase.

The PPC has a large absorption coefficient in the UV region, which is larger than that of the VIS region. The relatively high reflectance losses in the short wavelength region arise because of the refractive index mismatch between the covered layer and the FTO substrate, which reduces the actual number of photons going into the PPC absorber layer. The RE-GG is composed of inorganic oxide compounds with a relatively high refractive index. The difference in the
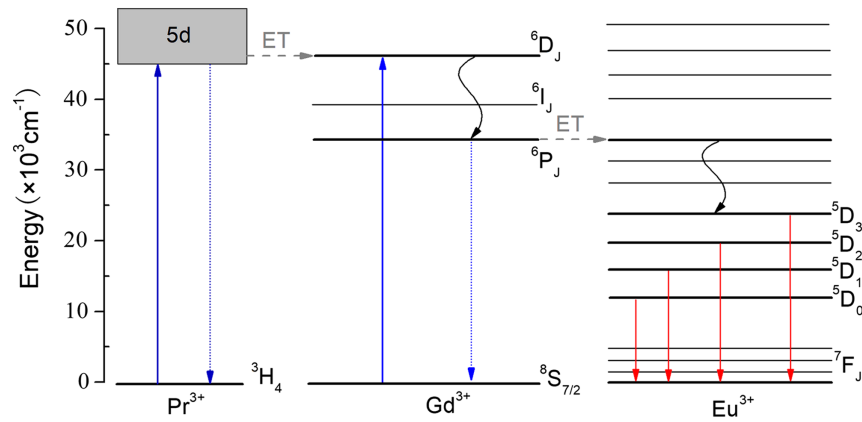
Fig. 7 ET diagram of the $GdPO_4$: Pr^{3+}-Eu^{3+} sample.
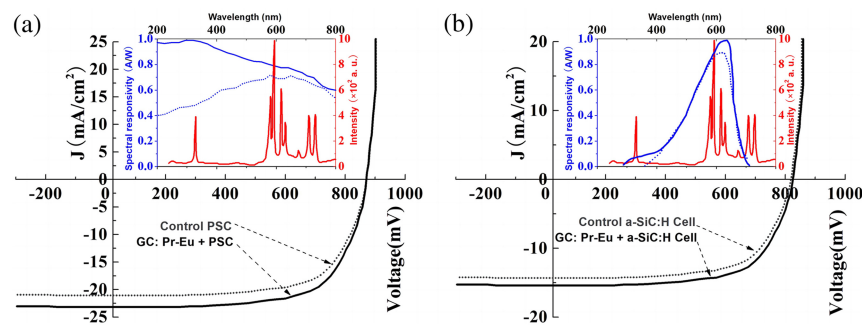
Fig. 8 Measured $J - V$ characteristic curves of PCs with the GC and the RE-free GC at $t = 0$ h. (a) For the PPC device and (b) for the a-SiC:H PC device. Inset shows the PL emission of the $GdPO_4$: Pr^{3+}-Eu^{3+} system, and the matching SR of (a) control PPC (blue dotted curve), PPC with GC (blue solid curve), (b) control a-SiC:H PC (blue dotted curve), and a-SiC:H PC with GC (blue solid curve).

refractive index between the GG layer and the substrate of the PC may result in significant losses (near 17%) in the device performance in the case of the a-SiC:H PC. The refractive index of the GG layer is approximately the same value as the FTO substrate of PPC, leading to comparatively lesser losses. In our case, the IMLIO, which is approximately the same value as the GC layer and the substrate, is applied. A majority of the UV photons are absorbed near the FTO-PPC interface and hence produce charge carriers mainly near this interface due to the high absorption coefficient of PPCs for short wavelengths. The above combined effects lower the short wavelength SR of PPCs. However, the DS of UV light to the VIS region provides a better spectral matching, and a greater number of charge carriers are generated away from the FTO-PPC interface. Therefore, an improvement in short wavelength SR is obtained. The photo-current improvement by DS-GC is an additional benefit considering the enhanced long-term stability of the PPC as a result of the absorption of harmful UV light and subsequent VIS emission. For PPCs, GC layers have dual benefits of enhancing in the photo-current and improving the UV stability. The a-SiC:H PC has a maximum absorption in VIS light of solar radiation. The GC simultaneously absorbs UV solar photons and then emits VIS photons, which is in the SR region of the a-SiC:H PC. Incident light harvesting is critical for the PCE for a-SiC:H PCs. As the result of above effect, more matched absorbable-photons could be used by the a-SiC:H PC, and the PCE can be greatly enhanced.

For evaluating UV photo-degradation effects on PPCs, the electrical parameters measurements including the photo-current (J_{sc}), the PCE (η), the open circuit voltages (V_{oc}), and fill factors (FFs), which were taken every 2 h from 0 to 16 h at a temperature of 20°C to 25°C and relative humidity of 30% to 40%. Normalized parameters J_{sc} and η of control PPC and GC-PPC as a function of illumination time are shown in Figs. 9(a) and 9(b). As shown in Fig. 9(a), the use
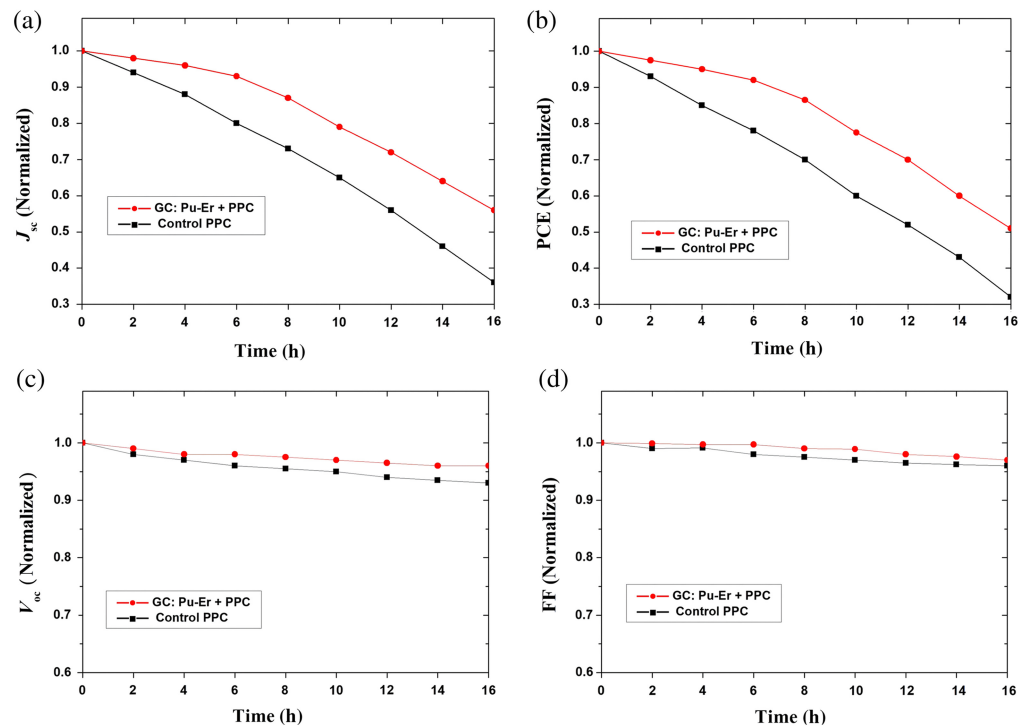
Fig. 9 Variation of electrical parameters of the PPC with the illumination time. Measurements were taken every 2 h at 20°C to 25°C and a relative humidity of 30% to 40%. (a) Normalized J_{sc}–time, (b) normalized PCE–time plots, (c) normalized V_{oc}–time plots, and (d) normalized FF–time plots for control PPC (black squares) and for GC-PPC (red circles).

of the GC layer (UV filter) led to a slight decrease in the photo-current (J_{sc}) value of the PPC. For control PPC, after 4 h of illumination without UV filtration, the photo-current value decreases to 88% of its original value, whereas for GC-PPC the photo-current value drops to around 96% of its initial value, indicating that there is virtually no change in the J_{sc} value. GC-PPC shows better photo-current behavior than the control PPC, leading to a comparatively lesser decrease in the PCE, as shown in Fig. 9(b). The PCE of control PPC drops to more than 50% and degrades to 32% of its initial value after 16 h, whereas the PCE of GC-PPC shows a much better performance, remaining at 51% of its original value at 16 h. This is a clear indication of UV degradation trouble for PPCs, but more importantly, it demonstrates the ability of GC materials to reduce the UV degradation. As also shown in Fig. 9(a), although the GC layer can arrest UV degradation of the PPC, the overall photo-current of GC-PPC starts to get lower than it was at 0 h. This phenomenon may be explained as follow: considering one aspect, the GC layer cannot entirely recycle incident UV photons owing to the improper layer thickness or unoptimized doping concentration. Considering a second aspect, GC-PPC units were not encapsulated in our test; therefore, PPCs may suffer from degradation due to environmental factors including moisture and oxygen. We found that the V_{oc} and FFs of control PPC (without UV filter) and GC-PPC (with UV filter) do not show a significant decline, as shown in Figs. 9(c) and 9(d). For a-SiC:H PCs, the electrical parameters J_{sc} and η of control PC and GC-PC do not show a significant decline mainly due to having no UV degradation defects. The GC-a-SiC:H PC shows better photo-current behavior and higher PCE values than the control a-SiC:H PC owing to it absorbing additional VIS photons provided by GCs and giving rise to the J_{sc} value improvement. For these two types of PCs, it can be understood that the electrical parameters V_{oc} and FF of control PC and GC-PC show a slight attenuation instead of a significant decline because the CG layer only changes the distribution of the incident photon flux, to connect directly with the generation of carrier densities, and leads to the increase of J_{sc} in the PCs without changing the diode property of the PCs.[33]

The measured performance of cell modules at $t = 0$ h is shown in Table 1. The use of DS-GC is shown to result in the improvement of short wavelength SR because a part of the UV

Table 1 Performance of RE-free GC and RE-GC covered PC modules at $t = 0$ h

Device type	J_{sc} (mA/cm^2)	V_{oc} (mV)	FF (%)	η (%)	$\Delta\eta$ (%)
Non-covered PPC	23.46	881	69.48	14.36	—
RE-free GC + PPC (control cell)	21.02	879	69.27	12.80	—
RE-GC + PPC	23.03	882	69.36	14.09	10.08
Non-covered a-SiC:H PC	16.83	811	63.01	8.60	—
RE-free GC + a-SiC:H PC (control cell)	14.51	808	62.09	7.28	—
RE-GC + a-SiC:H PC	15.53	812	63.17	7.96	9.34

radiation is converted to the VIS region, which is then absorbed by cell devices. The V_{oc} and FFs of the two kinds of PCs do not show a significant improvement. The relative PCE of the cell module is defined as the ratio of the PCE of the cell module with a Pr^{3+}-Eu^{3+}-doped GC sample to the PCE of the same cell with a RE-free GC sample (labeled as the control cell). For the PPC with GC, it shows an enhancement of 9.56% in the photo-current and 10.08% in PCE. For the a-SiC:H PC with GC, it shows an enhancement of 7.03% in the photo-current and 9.34% in PCE. The enhanced photo-current is primarily due to the enhancement in the 500 to 600 nm wavelength region, although a small increase is seen in the whole solar spectrum. As we know that the solar spectrum in space shows a strong UV absorption ranging from 200 to 300 nm, upon UV excitation around 220 nm and the DS effects, these results suggest that CG materials can simultaneously prevent the thermalization and enhance the PCE, making it a more promising candidate for a spectral converter for space PCs.

We found that the application of SCMs led to a slight decrease in the short-circuit current density (J_{sc}) value of the PC, which resulted in lower PCE when compared with the cell without any covered glass. But the use of SCMs lead to a better J_{sc} value when compared with cells covered with an UV filter or protective glass. In commercial applications, UV filters or protective glasses must be equipped with cell modules to prevent moisture, UV radiation, and impact. Therefore, there is still an added value of using an SCM as the PC performance has a slight improvement than non-covered PCs.

A proper thickness of the GC layer is required if the benefits of DS are to be fully realized. At this thickness, the GC layer should have a better absorption coefficient in the UV band/better quantum efficiency (QE) and better transmittance in the VIS band/better emission spectrum. The QE is related to both thickness and ions concentration, and the QE is increased as doping concentration increases until concentration-quenching occurs.[33] Doping levels of RE dopants were all fixed at $2\,Pr^{3+} - 1Eu^{3+}$ mol. % in our samples, and concentration quenching cannot occur at this time. We prepared some different thickness samples including 2, 3, 4, and 5 mm. On the one hand, a smaller thickness of the GC layer results in a higher transmittance, but photo-current enhancement and device stability cannot be improved because of insufficient DS of UV photons. On the other hand, a larger thickness of the GC layer results in a significant decrease in the transmittance value, and interface reflection and side scatting losses will reduce the efficiency of the PC. We found that the optical transmittance always decreases as the thickness increases from 2 to 5 mm, and the QE improves as the thickness increases from 2 to 4 mm, but the QE no longer increases as the thickness increases to 5 mm. This shows that the optical transmittance decreases more promptly with increasing the thickness. The PCE is improved as the thickness increases from 2 to 3 mm, and it begin to decrease when the 4 mm sample is applied. This shows that a thinner thickness and a higher concentration may be a good option. We optimized the thickness of 2 mm to obtain a better performance. In actual equipment, a smaller thickness perhaps cannot meet the strength requirements, whereas a larger thickness cannot meet the load or cost requirements. Therefore, there still can be a rather optimistic application foreground for the two kinds of PCs based on the control of several loss factors and the balance of cost-effectiveness in further research.

Currently, the expanding space stations require more power support and need high-performance PCs. As a type of broader light-absorption and higher efficiency PC, PPCs are a good option. But as mentioned before, PPCs have serious degradation problems due to environmental factors including UV, moisture, and oxygen. Fortunately, moisture and oxygen are extremely low in space, and we mainly need to solve the problem of UV exposure. Technical solutions of UV filters that we adopt can solve the problem and realize the reuse of ultraviolet photons. $GdPO_4$-GC-SCM can keep high thermal and chemical stabilities in space. If the SCM covers the top side of the PPC, using a properly encapsulated and sealing technology, it ensures very low humidity levels and achieves UV recycling. In addition, the GC material has a hard texture, so it can well protect PCs from being hit by tiny floating debris in space. As non-flexible modules, it is more suitable for use as stationary units on space stations instead of as flexible or foldable units on satellites.

4 Conclusion

$GdPO_4$-GC: Eu^{3+}/Pr^{3+} with perfect dispersibility of RE ions and ideal optical properties was successfully synthesized by the MQ technique. Obvious VIS-red fluorescence emissions were observed in the GC sample under the excitation of UV radiation. The investigated spectral properties confirmed the remarkable energy transfer from the Pr^{3+} ion to the Gd^{3+} ion by the bridge Gd^{3+} ion in $GdPO_4$-GC, and intense VIS fluorescence emissions were observed. The present study exhibits a simple technique involving a top covered transparent $GdPO_4$-GC: Eu^{3+}/Pr^{3+} that contains the dual functions of improving the UV-stability for PPC and enhancing the efficiencies for two types of PCs. The efficiencies of PPC and a-SiC:H PC are effectively enhanced due to the optimized spectral distribution. The present work provides a potential application toward terrestrial PCs and space PCs.

Code and Data Availability

All data in support of the findings of this paper are available within the article.

References

1. B. S. Richards, "Enhancing the performance of silicon solar cells via the application of passive luminescence conversion layers," *Sol. Energy Mater. Sol. Cells* **90**(15), 2329–2337 (2006).
2. V. Avrutin, N. Izyumskaya, and H. Morkoc, "Semiconductor solar cells: recent progress in terrestrial applications," *Superlattices Microstruct.* **49**(4), 337–364 (2011).
3. L. Etgar et al., "Mesoscopic $CH_3NH_3PbI_3/TiO_2$ heterojunction solar cells," *J. Am. Chem. Soc.* **134**, 17396–17399 (2012).
4. H. S. Kim et al., "Lead iodide perovskite sensitized all-solid-state submicron thin film mesoscopic solar cell with efficiency exceeding 9%," *Sci. Rep.* **2**, 591 (2012).
5. M. M. Lee et al., "Efficient hybrid solar cells based on meso-superstructured organometal halide perovskites," *Science* **338**(6107), 643–647 (2012).
6. T. Leijtens et al., "Overcoming ultraviolet light instability of sensitized TiO_2 with meso-superstructured organometal tri-halide perovskite solar cells," *Nat. Commun.* **4**(1), 2885 (2013).
7. G. D. Niu et al., "Study on the stability of $CH_3NH_3PbI_3$ films and the effect of post-modification by aluminum oxide in all-solid-state hybrid solar cells," *J. Mater. Chem. A: Mater. Energy Sustain.* **2**(3), 705–710 (2014).
8. M. A. Green et al., "Solar cell efficiency tables (version 49)," *Prog. Photovolt. Res. Appl.* **24**, 905–913 (2016).
9. M. Ahmadi et al., "Effect of photogenerated dipoles in the hole transport layer on photovoltaic performance of organic–inorganic perovskite solar cells," *Adv. Energy Mater.* **7**(4), 1601575 (2017).
10. W. S. Yang et al., "Iodide management in formamidinium-lead-halide-based perovskite layers for efficient solar cells," *Science* **356**(6345), 1376–1379 (2017).
11. C. Chen et al., "Carrier interfacial engineering by bismuth modification for efficient and thermoresistant perovskite solar cells," *Adv. Energy Mater.* **8**(20), 1703659 (2018).

12. J. Burschka et al., "Sequential deposition as a route to high-performance perovskite-sensitized solar cells," *Nature* **499**(7458), 316–319 (2013).
13. J. De Wild et al., "Towards upconversion for amorphous silicon solar cells," *Sol. Energy Mater. Sol. Cells* **94**(11), 1919–1922 (2010).
14. W. Van Sark et al., "Enhancing solar cell efficiency by using spectral converters," *Sol. Energy Mater. Sol. Cells* **87**(1), 395–409 (2005).
15. P. Song, C. M. Zhang, and P. F. Zhu, "Eu^{3+}-Mn^{2+}-doped bi-functional glasses with solar photon downshifting: application to CdS/CdTe solar cells," *J. Alloys Compd.* **661C**, 14–19 (2016).
16. O. Morton, "Solar energy: a new day dawning? Silicon valley sunrise," *Nature* **443**(7107), 19–22 (2006).
17. A. Goetzberger, C. Hebling, and H. W. Schock, "Photovoltaic materials, history, status and outlook," *Mater. Sci. Eng: R* **40**, 1–46 (2003).
18. N. S. Lewis and D. G. Nocera, "Powering the planet: chemical challenges in solar energy utilization," *Proc. Natl. Acad. Sci. U. S. A.* **103**(43), 15729–15735 (2006).
19. B. van der Zwaan and A. Rabl, "Prospects for PV: a learning curve analysis," *Sol. Energy* **74**, 19–31 (2003).
20. C. K. Huang et al., "Enhanced light harvesting of Si solar cells via luminescent down-shifting using $YVO_4 : Bi^{3+}$, Eu^{3+} nanophosphors," *Prog. Photovolt. Res. Appl.* **21**(7), 1507–1513 (2013).
21. E. Klampaftis and B. S. Richards, "Improvement in multi-crystalline silicon solar cell efficiency via addition of luminescent material to EVA encapsulation layer," *Prog. Photovolt. Res. Appl.* **19**(3), 345–351 (2011).
22. D. Alonso-Álvarez et al., "Luminescent down-shifting experiment and modelling with multiple photovoltaic technologies," *Prog. Photovolt. Res. Appl.* **23**(4), 479–497 (2015).
23. H. Li et al., "Near-infrared and ultraviolet to visible photon conversion for full spectrum response perovskite solar cells," *Nano Energy* **50**, 699–709 (2018).
24. R. Tao et al., "Lanthanide-containing polyoxometalate as luminescent down-conversion material for improved printable perovskite solar cells," *J. Alloys Compd.* **823**, 153738 (2020).
25. T. Trupke et al., "Efficiency enhancement of solar cells by luminescent up-conversion of sunlight," *Sol. Energy Mater. Sol. Cells* **90**(18-19), 3327–3338 (2006).
26. T. Trupke, M. A. Green, and P. Wurfel, "Improving solar cell efficiencies by up-conversion of sub-band-gap light," *J. Appl. Phys.* **92**(7), 4117–4122 (2002).
27. T. Trupke, M. A. Green, and P. Wurfel, "Improving solar cell efficiencies by down-conversion of high-energy photons," *J. Appl. Phys.* **92**(3), 1668–1674 (2002).
28. B. S. Richards, "Luminescent layers for enhanced silicon solar cell performance: down-conversion," *Sol. Energy Mater. Sol. Cells* **90**(9), 1189–1207 (2006).
29. R. E. Bird et al., "Solar spectral measurements in the terrestrial environment," *Appl. Opt.* **21**(8), 1430–1436 (1982).
30. X. Y. Zhang et al., "Efficient deep ultraviolet to near infrared quantum cutting in Pr^{3+}/Yb^{3+} codoped $CaGdAlO_4$ phosphors," *J. Alloys Compd.* **740**, 595–602 (2018).
31. V. G. Litovchenko et al., "Nitrogen containing diamond-like carbon films as protective and fluorescent layers for silicon solar cells," *Opto-Electron. Rev.* **8**(4), 402–405 (2000).
32. A. U. Rehman, S. H. Lee, and S. H. Lee, "Silicon space solar cells: progression and radiation-resistance analysis," *J. Kor. Phys. Soc.* **68**(4), 593–598 (2016).
33. P. Song and C. Jiang, "Modeling of quantum cutting systems in Tm^{3+}/Yb^{3+}-codoped spectral converters for sc-Si solar-cell efficiency enhancement," *IEEE Photonics J.* **4**(6), 2143–2151 (2012).

Biographies of the authors are not available.